International Journal of Computational Materials Science and Engineering

FINITE ELEMENT ANALYSIS OF 3D-PRINTED ACRYLONITRILE STYRENE ACRYLATE (ASA) WITH ULTRASONIC MATERIAL CHARACTERIZATION

YEE LING YAP*, WILLIAM TOH[#], RAHUL KONERU, ZHONG YANG CHUA

Singapore Centre for 3D Printing, Nanyang Technological University, 50 Nanyang Avenue, N3.1-B2C-03 Singapore 639798
ylyap@e.ntu.edu.sg

KEHUA LIN, KIRK MING YEOH, CHIN MIAN LIM, JIA SHING LEE, NUR ADILAH PLEMPING, RONGMING LIN, TENG YONG NG

School of Mechanical and Aerospace Engineering, Nanyang Technological University, 50 Nanyang Avenue, Singapore 639798
[#]williamtoh@ntu.edu.sg

KEEN IAN CHAN, HUANYU GUANG, WAI YEW BRIAN CHAN, SOO SOON TEONG, GUOYING ZHENG

ST Engineering Aerospace Ltd., 540 Airport Road, Singapore 539938

Received Day Month Year
Revised Day Month Year

This paper investigates the orthotropic properties of Fused Deposition Modelling (FDM) printed ASA material with different raster configurations. The elastic properties were determined using a non-destructive ultrasonic technique. This technique allows us to deduce the orthotropic elastic constants from the material density and the velocities of the longitudinal and shear wave propagating through the material along different directions. Tensile tests were performed in addition to ultrasonic tests to obtain the yield properties of the ASA material and to validate the elastic constants determined by the ultrasonic tests, which have shown very close correspondence. Finally, numerical verification was performed by comparing the experimental result of the three-point and four-point bending tests with the finite element simulation results which have input the material properties from the ultrasonic testing. The simulation result has shown excellent agreement with the experimental result, implying that the material properties obtained from the ultrasonic testing were highly accurate comparing to the actual orthotropic elastic properties of the 3D printed ASA material.

Keywords: finite element modeling; additive manufacturing; ASA; fused deposition modelling; ultrasonic testing; orthotropic properties.

1. Introduction

3D Printing, or additive manufacturing (AM), is an advanced manufacturing technique that allows rapid prototyping of complex and difficult-to-machine parts and enables the user to materialize a computer-aided design (CAD) into reality. AM reduces production costs and shortens manufacture time and cost for complex prototype designs that would otherwise require expensive moulds [Baumers et al., 2016; Vashishtha et al., 2011]. Fused Deposition Modelling (FDM) is an AM technique which involves the melting and extrusion of a

filament material at specific intervals and predetermined locations where it cools and solidifies, one layer at a time. Due to the layer-by-layer building mechanism, part orientation plays a significant role in the mechanical properties, dimensional accuracy and surface finish. In addition, other building parameters in FDM, such as raster angle, also contribute to the anisotropic material properties [Cantrell et al., 2017; Wu et al., 2015]. Numerous research on the elastic properties has been carried out on many FDM-printed materials including acrylonitrile butadiene styrene (ABS) [Dawoud et al., 2016; Sood et al., 2010], polylactic acid (PLA) [Chacón et al., 2017; Odell et al., 2002] and polycarbonate (PC) [Cantrell et al., 2017; Domingo-Espin et al., 2015]. However, there is limited report on the full orthotropic properties of 3D printed materials, which are essential for designing structural components using numerical simulation. This has thus resulted in the limited usage of designing 3D printed components using computer simulations.

Mechanical testing, such as tensile, compression, flexural testing, are often used to characterize the elastic properties of 3D printed orthotropic materials [Chua et al., 2017]. Due to the destructive nature of mechanical testing, there is usually excessive material wastage during characterization. In this paper, a non-destructive ultrasonic testing is adopted to characterize the anisotropic elastic constants of the 3D printing materials. This technique was initially used for characterizing bones, rocks and other composites that do not possess fixed shape or have constraints in the size of specimens. The elastic constants can be deduced from the bulk density and the velocities of shear and longitudinal ultrasound wave propagating along different directions through a single specimen [Lang, 1970; Peralta et al., 2017; Van Buskirk et al., 1981].

This paper investigates the elastic properties of the ASA material printed by FDM 3D printer using the non-destructive ultrasonic testing approach. Ultrasonic test was performed on the ASA specimens that have 0° and 0°/90° raster, to determine their elastic constants of these orthotropic ASA materials. In addition, tensile tests were carried out to compare the elastic constants and to obtain the yield properties of ASA materials. Finally, the orthotropic elastic properties obtained by the ultrasonic test were used in the finite element simulation for three-point and four-point bending tests. The numerical verifications show that there is excellent agreement between the experimental and finite element simulation results.

2. Theory

2.1. *Orthotropic Constitutive Model*

The elastic properties of a materials can be described by the generalized Hooke's Law relating stresses to strains (Equation 1).

$$\sigma_i = c_{ij}\epsilon_j \quad (1)$$

For an orthotropic material, the stiffness matrix, c_{ij}, has nine independent elastic constants, as shown in Equation (2).

$$[c_{ij}] = \begin{bmatrix} c_{11} & c_{12} & c_{13} & 0 & 0 & 0 \\ c_{12} & c_{22} & c_{23} & 0 & 0 & 0 \\ c_{13} & c_{23} & c_{33} & 0 & 0 & 0 \\ 0 & 0 & 0 & c_{44} & 0 & 0 \\ 0 & 0 & 0 & 0 & c_{55} & 0 \\ 0 & 0 & 0 & 0 & 0 & c_{66} \end{bmatrix} \quad (2)$$

The strain-stress relationships of an orthotropic material can be written in terms of a compliance matrix s_{ij} such that

$$\varepsilon_i = s_{ij}\sigma_j \quad (3)$$

where $\varepsilon_i = \begin{bmatrix} \varepsilon_x & \varepsilon_y & \varepsilon_z & \gamma_{yz} & \gamma_{xz} & \gamma_{xy} \end{bmatrix}^T$ is the strain,

$\sigma_i = \begin{bmatrix} \sigma_x & \sigma_y & \sigma_z & \tau_{yz} & \tau_{xz} & \tau_{xy} \end{bmatrix}^T$ is the stress, and

$$[s_{ij}] = \begin{bmatrix} s_{11} & s_{12} & s_{13} & 0 & 0 & 0 \\ s_{12} & s_{22} & s_{23} & 0 & 0 & 0 \\ s_{13} & s_{23} & s_{33} & 0 & 0 & 0 \\ 0 & 0 & 0 & s_{44} & 0 & 0 \\ 0 & 0 & 0 & 0 & s_{55} & 0 \\ 0 & 0 & 0 & 0 & 0 & s_{66} \end{bmatrix} = \begin{bmatrix} \frac{1}{E_1} & \frac{-\nu_{21}}{E_2} & \frac{-\nu_{31}}{E_3} & 0 & 0 & 0 \\ \frac{-\nu_{12}}{E_1} & \frac{1}{E_2} & \frac{-\nu_{32}}{E_3} & 0 & 0 & 0 \\ \frac{-\nu_{13}}{E_1} & \frac{-\nu_{23}}{E_2} & \frac{1}{E_3} & 0 & 0 & 0 \\ 0 & 0 & 0 & \frac{1}{G_{23}} & 0 & 0 \\ 0 & 0 & 0 & 0 & \frac{1}{G_{31}} & 0 \\ 0 & 0 & 0 & 0 & 0 & \frac{1}{G_{12}} \end{bmatrix}.$$

From symmetry of the compliance matrix,

$$\frac{\nu_{12}}{E_1} = \frac{\nu_{21}}{E_2}, \frac{\nu_{13}}{E_1} = \frac{\nu_{31}}{E_3}, and\ \frac{\nu_{23}}{E_2} = \frac{\nu_{32}}{E_3} \quad (4)$$

2.2. *Ultrasonic wave and elastic properties*

The equations relating to the components in the stiffness matrix and the wave velocities are shown in Equations (5) to (13).

$$c_{11} = \rho v_1^2 \quad (5)$$

$$c_{22} = \rho v_2^2 \quad (6)$$

$$c_{33} = \rho v_3^2 \quad (7)$$

$$c_{44} = \rho v_{23}^2 = \rho v_{32}^2 \quad (8)$$

$$c_{55} = \rho v_{13}^2 = \rho v_{31}^2 \quad (9)$$

$$c_{66} = \rho v_{12}^2 = \rho v_{21}^2 \quad (10)$$

$$c_{12} = \sqrt{\left(c_{11} + c_{66} - 2\rho v_{12/12}^2\right)\left(c_{22} + c_{66} - 2\rho v_{12/12}^2\right)} - c_{66} \quad (11)$$

$$c_{13} = \sqrt{\left(c_{11} + c_{55} - 2\rho v_{13/13}^2\right)\left(c_{33} + c_{55} - 2\rho v_{13/13}^2\right)} - c_{55} \quad (12)$$

$$c_{23} = \sqrt{\left(c_{22} + c_{44} - 2\rho v_{23/23}^2\right)\left(c_{33} + c_{44} - 2\rho v_{23/23}^2\right)} - c_{44} \quad (13)$$

where

v_i denotes the velocity of a longitudinal wave in direction *i*,

v_{ij} denotes the velocity of transverse wave travelling in direction *i*, with particle displacements in direction *j*,

$v_{ij/k}$ denotes the velocity of a transverse wave travelling in direction (*i*+*j*)/2 with particle displacements in direction *k*,
$v_{ij/ij}$ denotes the velocity a transverse or longitudinal wave travelling in direction (*i*+*j*)/2 with particle displacements in the *i*-*j* plane. Velocities are quasi-longitudinal or quasi-transverse,
ρ represents the density of the material.

The components in the compliance matrix s_{ij}, and thus the elastic constants, can be obtained through the inverse relation with the stiffness matrix.

$$[s] = [c]^{-1} \quad (14)$$

3. Materials and Experimental Procedures

3.1. *Materials and Printing Configurations*

The Stratasys Fortus 450mc fitted with T12 model tip and T12SR100 support tip was used to print the Acrylonitrile Styrene Acrylate (ASA) specimen. Other build parameters are listed in Table 1.

Table 1 Build Parameter of ASA.

Raster width (mm)	Contour width (mm)	Slice height (mm)	Air gap (mm)
0.3556	0.3556	0.1778	0

Two types of raster, namely the 0° raster and the alternating layers of 0°/90° were investigated in this paper, the raster layouts are illustrated in Figure 1. The longitudinal direction of the tensile specimen is parallel to the 3D printer's X-, Y- and Z-axes.
The alternating 0°/90° raster in X- and Y-orientations are assumed to be transversely isotropic because the 0° and 90° rasters are identical with 90° rotation. Hence only 2 orientations, X and Z orientations, are required for determination of the elastic constants for 0°/90° configuration.

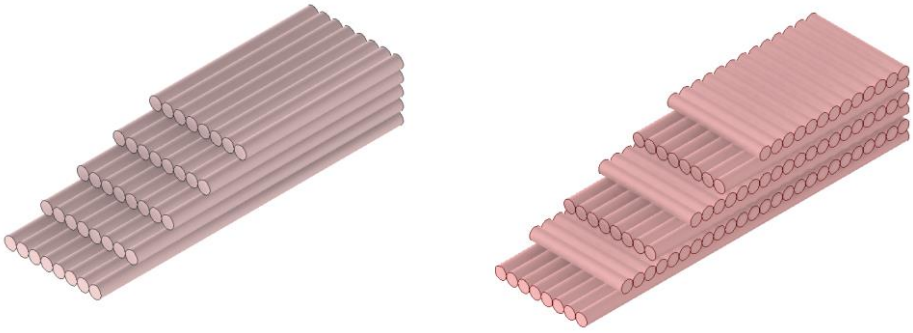

(a) (b)

Figure 1 Raster configuration: (a) 0° and (b) 0°/90° with alternating layer of 0° and 90° raster

3.2. *Ultrasonic Testing*

To measure the 9 wave velocities, two types of specimens, cubic and oblique specimens, as shown in Figure 2(a) and (b), were designed. The cubic specimen in Figure 2(a) was used to measure v_i and v_{ij} while the oblique specimen in Figure 2(b) has faces with unit normal $n_1 = \pm(e_2 + e_3)/\sqrt{2}$, $n_2 = \pm(e_1 + e_3)/\sqrt{2}$ and $n_3 = \pm(e_1 + e_2)/\sqrt{2}$ was used to measure $v_{ij/k}$ and $v_{ij/ij}$. Two specimens of cubic and oblique specimens were built for each raster.

Both the specimens were designed with a constant thickness of 10 mm and the dimensions according to Figure 2 based on the size of the chosen transducers and the attenuation of sound wave in the ASA material. The thickness of each specimen was measured using a Vernier caliper before carrying out the ultrasonic test. Mass of the ASA specimens was measured using an electronic weight balance and the density was obtained by dividing the mass by the volume of specimen. The average density of ASA was found to be 1.016 g/cm^3. Pulsed transmission technique was used to measure the ultrasonic wave velocities. MultiX-LF low frequency parallel system with 16 channels and Multi2000 software were used in this study. A 5 MHz single element longitudinal wave transducer capable of generating and receiving the longitudinal waves were used together with GE ultrasonic testing couplant ZG-F. The wave velocity can be obtained from the time-of-flight of the first backwall echo and the specimen thickness.

On the other hand, a pair of 2.25MHz shear wave transducers was used to transmit and receive the transverse waves directly into the test specimen. The ultrasonic velocity can be calculated from the time delay of the propagation between the transmitted and received waves, and the specimen thickness.

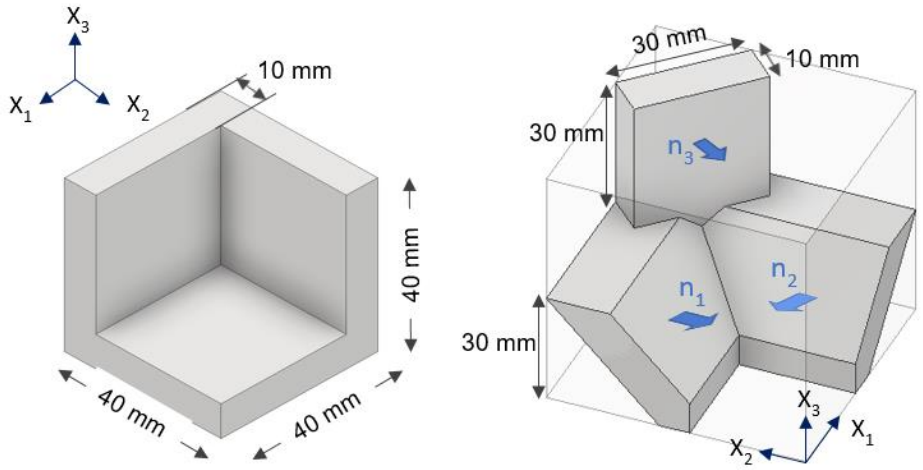

Figure 2 Specimens for ultrasonic testing: (a) cubic specimen for measuring v_i and v_{ij}, (b) oblique specimen which has faces with unit normal $n_1 = \pm(e_2 + e_3)/\sqrt{2}$, $n_2 = \pm(e_1 + e_3)/\sqrt{2}$ and $n_3 = \pm(e_1 + e_2)/\sqrt{2}$ for measuring $v_{ij/k}$ and $v_{ij/ij}$

3.3. *Mechanical Testing*

To verify the elastic constants, including the Young's moduli and Poisson's ratios of those obtained from ultrasonic testing, 5 tensile specimens for each orientation and each raster were designed, built and tested according to the ASTM D638 Standard Test Method for Tensile Properties of Plastics, where the specimen geometry follows the Type I specifications. The tensile tests were performed using Shimadzu AGS-10kNX universal testing machine with a crosshead displacement rate of 10 mm/min. Axial displacement was measured using Shimadzu mechanical extensometer. In addition, rectangular bars with dimensions of 165 mm x 20 mm x 3.2 mm were printed for determining the Poisson's ratio using the strain gauge GFCA-3-350-70. TDS-303 portable data logger was used to measure the axial and transverse strain during the elastic tensile loading. For every orientation and every raster, 5 specimens were printed and strain measurements were repeated 3 times for every specimen. Instead of finding all the six Poisson's ratios, only ν_{12}, ν_{31} and ν_{23} are required for the 0° raster because of the symmetry of the compliance matrix as shown in Equation 5. For 0°/90° raster, only two Poisson's ratios, ν_{12} and ν_{31}, are needed.

4. Results and Discussion

4.1. *Ultrasonic results*

The stiffness coefficients can be derived using the measured wave velocities using Equations 5-13. The elastic constants were hence calculated using Equation 3, using the inverse of the stiffness matrix (Equation 14). Elastic properties of ASA in raster 0° and 0°/90° are shown in Table 2. The ultrasonic results in Table 2 confirm that 0°/90°

configurations are transversely isotropic as expected as $E_1 \approx E_2$, $G_{13} \approx G_{23}$, and $\nu_{13} \approx \nu_{23}$.

Table 2 Mean elastic constants for raster 0° and 0°/90° obtained from ultrasonic testing

Elastic Constant	0°	0°/90°
E_1 (GPa)	2.37	2.17
E_2 (GPa)	1.94	2.21
E_3 (GPa)	1.93	1.96
G_{23} (GPa)	0.71	0.76
G_{13} (GPa)	0.77	0.75
G_{12} (GPa)	0.79	0.79
ν_{12}	0.397	0.380
ν_{21}	0.326	0.386
ν_{31}	0.340	0.355
ν_{13}	0.419	0.395
ν_{23}	0.372	0.379
ν_{32}	0.369	0.336

4.2. *Tensile Results*

The mean and standard deviation of the Young's modulus, yield strength, elongation at yield, ultimate tensile strength and maximum elongation are shown in Table 3. The stress-strain curves of these configurations are displayed in Figure 3.

The X-orientation exhibited the highest tensile properties among all the orientations. This can be attributed to how the main load bearing raster is oriented with respect to the direction of loading. In the case of the X-0° configuration, it is the individual raster that bears the tensile load while for the X-0°/90° configuration, the tensile load is shared between the bonding within the raster itself and the individual rasters. Hence, lower Young's modulus and yield strength were obtained from the X-0°/90° configuration. For Y-0° configuration, the adhesion between adjacent raster within one layer in the bears most of the load. Hence Y-0° configuration has much lower tensile properties than the X-orientation because of its weak raster-to-raster bonding. Z-orientation also demonstrated relatively weak tensile properties, and this might be caused by the weak inter-layer bonds bearing the tensile load. As opposed to the inter-raster adhesion acting as the main loading mechanism in the Y orientation, Z-orientation specimens' loading mechanism is the inter-layer adhesion. The layers are only fused together after the entire layer has been printed and cooled down in the Z-orientation, whereas the inter-raster bonds are formed immediately after the material is extruded from the nozzle for the Y-orientation.

The elastic constants extracted from the tensile test are shown in Table 4. For 0°/90° configurations, only 4 elastic constants were needed due to its symmetry in the raster layout.

Table 3 Means and standard deviations of Young's modulus, yield strength, elongation at yield, ultimate tensile strength and maximum elongation of ASA for each orientation and raster.

Orientation - Raster	Young's Modulus / GPa	Yield Strength / MPa	Elongation at yield / %	Ultimate Tensile Strength /MPa	Maximum elongation /%
X-0°	1.96 ± 0.08	30.5 ± 0.2	1.77 ± 0.05	34.0 ± 0.8	20.2 ± 0.5
X-0°/90°	2.05 ± 0.06	24.2 ± 0.3	2.8 ± 0.1	28.92 ± 0.09	2.8 ± 0.1
Y-0°	1.62 ± 0.06	18.3 ± 0.5	1.33 ± 0.04	23.1 ± 0.3	2.6 ± 0.2
Z-0°	1.79 ± 0.09	20.8 ± 0.4	1.35 ± 0.05	23.4 ± 0.8	1.8 ± 0.2
Z-0°/90°	1.93 ± 0.06	20 ± 2	1.1 ± 0.1	20 ± 2	1.1 ± 0.1

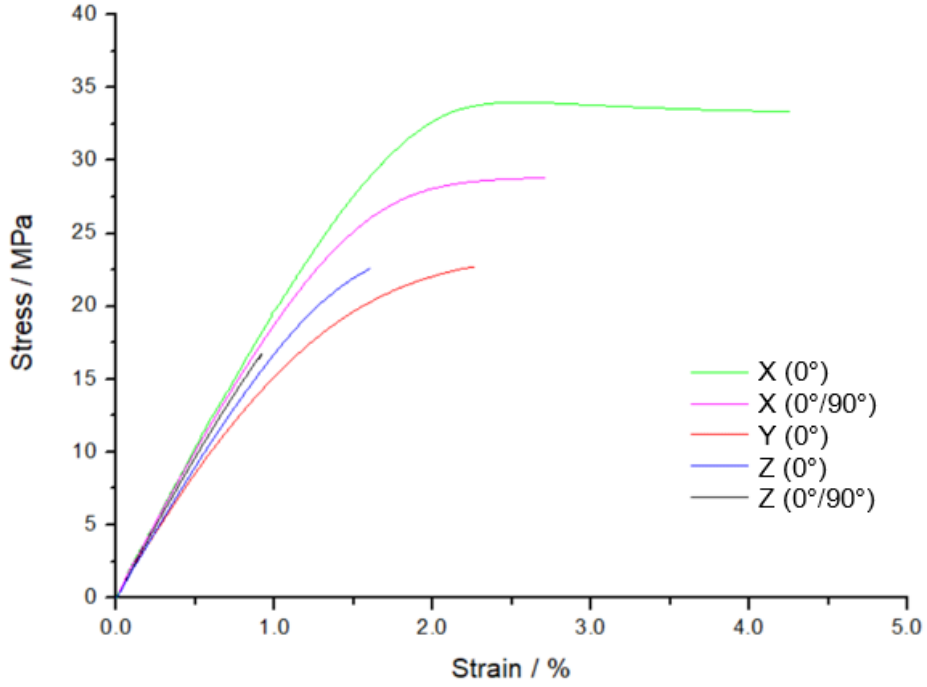

Figure 3 Average stress-strain curves for specimens with different orientations and raster configurations.

Table 4 Mean elastic constants and standard deviations for raster 0° and 0°/90° determined by tensile testing

Raster	E_1 (GPa)	E_2 (GPa)	E_3 (GPa)	ν_{12}	ν_{31}	ν_{23}
0°	1.96 ± 0.08	1.62 ± 0.06	1.79 ± 0.09	0.349 ± 0.006	0.324 ± 0.004	0.39 ± 0.01
0°/90°	1.99 ± 0.05	-	1.93 ± 0.06	0.367 ± 0.009	-	0.39 ± 0.01

4.3. *Comparison of elastic constants from tensile test and ultrasonic test*

Figure 4 shows the comparison of the elastic constants, namely the Young's moduli and Poisson's ratios, obtained from tensile tests and ultrasonic tests. As shown in Figure 4 (a) and Figure 4 (c), E_1, E_2 and E_3, as well as the Poisson's ratios, ν_{12}, ν_{31} and ν_{23}, obtained from ultrasonic tests are consistently higher than that obtained from tensile tests. This trend is expected because of the dynamic strain rate used in an ultrasonic test which causes the elastic constants measured by ultrasonic testing to be higher than that measured by mechanical testing with 0.0017 s^{-1} strain rate.

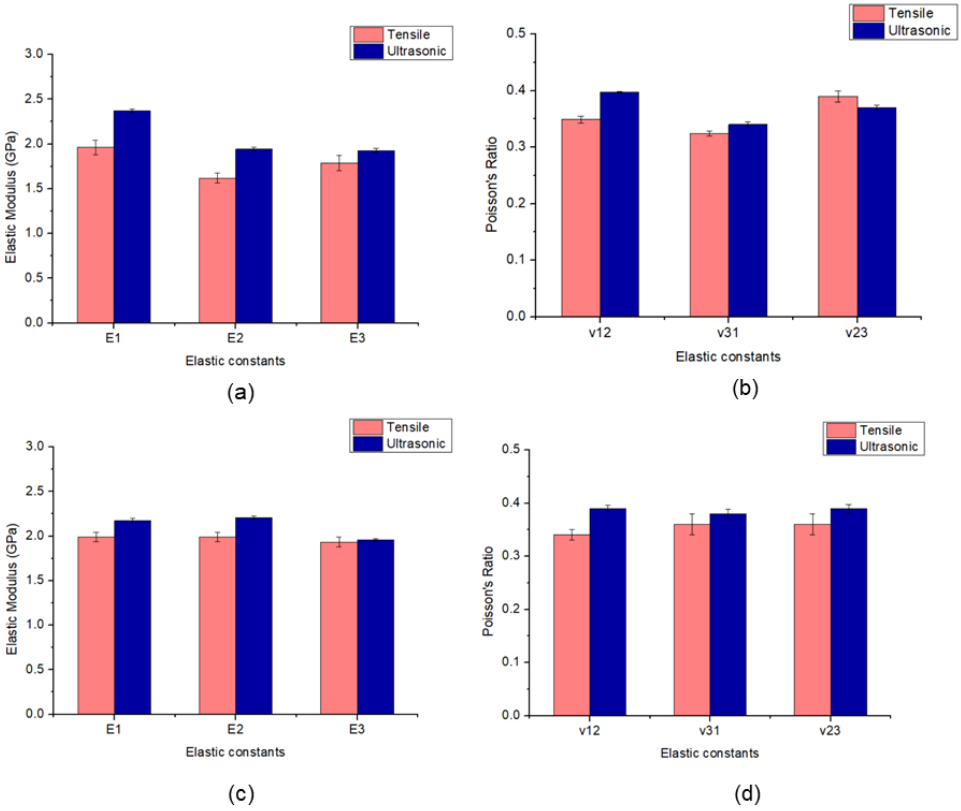

Figure 4 Comparison of the elastic constants of ASA obtained from tensile test and ultrasonic test (a) Elastic moduli for 0° raster, (b) Poisson's ratio for 0° raster, (c) Elastic moduli for 0°/90° raster, (d) Poisson's ratio for 0°/90° raster.

5. Numerical Verification using Finite Element Simulation

Numerical verification was performed using the three-point and four-point bending tests. The positioning of the test fixture and the dimensions of the tests are shown in Figure 5. To better verify the material properties, both test specimens were printed in 45°/-45° raster instead of 0°/90° raster obtained in the experimental characterization. This is because of

the coupled effects between the various elastic constants. A 0°/90° raster specimen in three-point bending is predominantly dependent on just the longitudinal Young's modulus E_1, whereas by simply printing the rasters with an in-plane rotation of 45°, the transformed longitudinal Young's modulus becomes dependent on the in-plane shear moduli and Poisson's ratios as well.The required material properties of the specimen were obtained after performing coordinate transformation equation $[\bar{s}]=[R][T]^{-1}[R]^{-1}[s][T]$ [Joshi and Toh, 2011] on the orthotropic linear elastic properties for 0°/90° raster. The components of the transformation equation are: the transformed and untransformed compliance matrix $[\bar{s}]$ and $[s]$ respectively, the transformation and the Reuter matrices $[T]$ and $[R]$ are shown in Equations 15 and 16, respectively.

$$[T]=\begin{bmatrix} \cos^2\theta & \sin^2\theta & 0 & 0 & 0 & 2\sin\theta\cos\theta \\ \sin^2\theta & \cos^2\theta & 0 & 0 & 0 & -2\sin\theta\cos\theta \\ 0 & 0 & 1 & 0 & 0 & 0 \\ 0 & 0 & 0 & \cos\theta & -\sin\theta & 0 \\ 0 & 0 & 0 & \sin\theta & \cos\theta & 0 \\ -\sin\theta\cos\theta & \sin\theta\cos\theta & 0 & 0 & 0 & \cos 2\theta \end{bmatrix} \quad (15)$$

$$[R]=\begin{bmatrix} 1 & 0 & 0 & 0 & 0 & 0 \\ 0 & 1 & 0 & 0 & 0 & 0 \\ 0 & 0 & 1 & 0 & 0 & 0 \\ 0 & 0 & 0 & 2 & 0 & 0 \\ 0 & 0 & 0 & 0 & 2 & 0 \\ 0 & 0 & 0 & 0 & 0 & 2 \end{bmatrix} \quad (16)$$

where θ the angle of in-plane rotation.

(a)

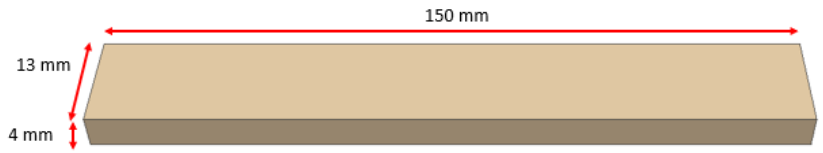

(b)

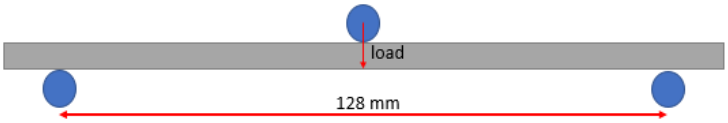

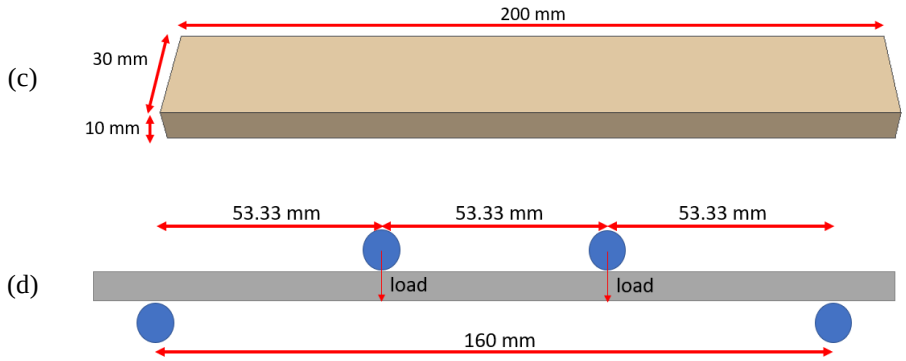

Figure 5: (a) Positioning of the test fixture and (b) dimensions of three-point bending specimen. Corresponding figures for four-point bending are shown in (c) and (d)

Table 5 shows the full orthotropic properties after transformation and used in simulation. In applying these orthotropic properties, the raster configuration has been taken into consideration, which is consistent with the theoretical analysis presented earlier in this Section.

Table 5 Orthotropic elastic constants of 45°/-45° raster of ASA

Elastic Constant	**45°/-45°**
E_1 (GPa)	2.1478
E_2 (GPa)	2.1478
E_3 (GPa)	1.9450
G_{23} (GPa)	0.7910
G_{13} (GPa)	0.7565
G_{12} (GPa)	0.7565
ν_{12}	0.3854
ν_{13}	0.3995
ν_{23}	0.3995

Figure 6 shows the experimental set-ups of both bending tests prior to any deformation. Figure 7 shows the finite element simulations of the deformed states and Mises stress of the test specimens. Simulation and experimental results are compared using the force-deflection relations in Figure 8. There is good correlation between the simulation and experiment results, implying that the orthotropic properties derived from the ultrasonic test were good representative of the actual orthotropic mechanical properties of the ASA material. However, it is to be noted that since only linear elastic material properties were assigned in the finite element model, the simulation is unable to predict the point of failure of the specimen.

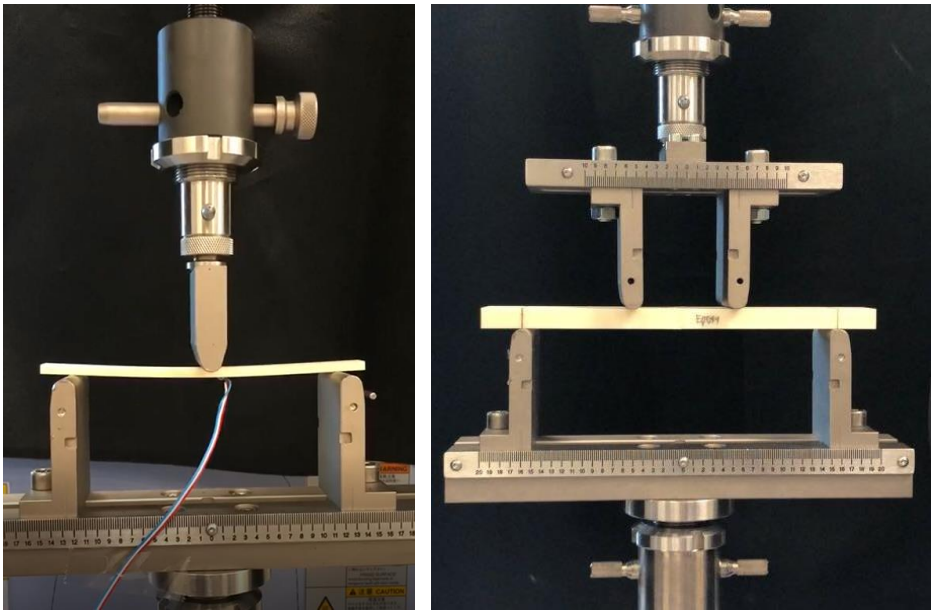

(a) (b)

Figure 6: Three-point bending test (a) before deflection, (b) after deflection of 12.8 mm and (c) shows the corresponding deformation and stress contour of finite element simulation results.

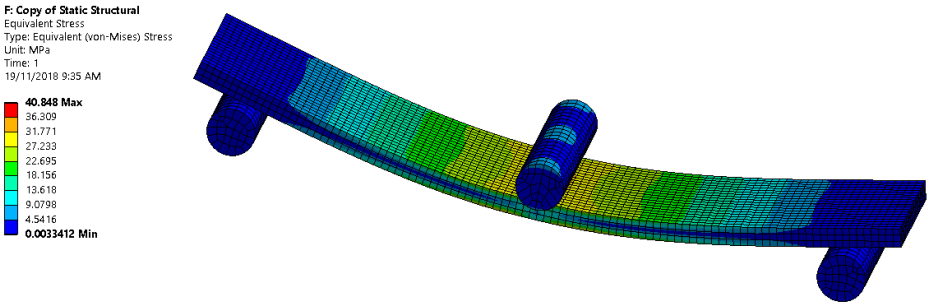

(a)

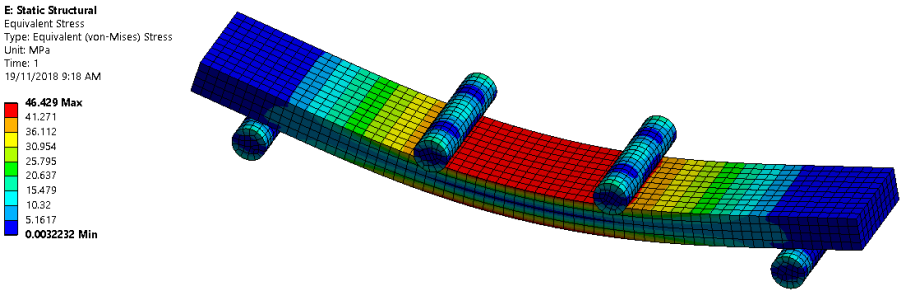

(b)

Figure 7: Mises stress in test specimens at 10 mm displacement of (a) three-point bending test, and (b) four-point bending test.

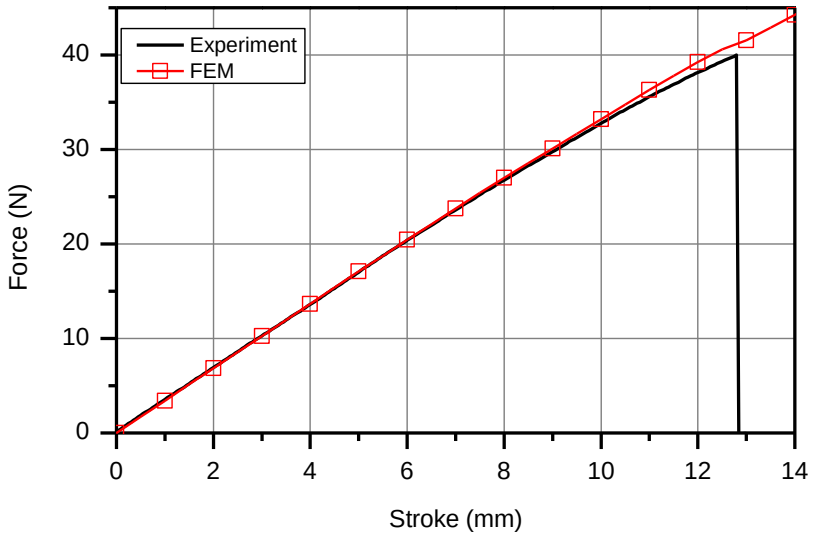

(a)

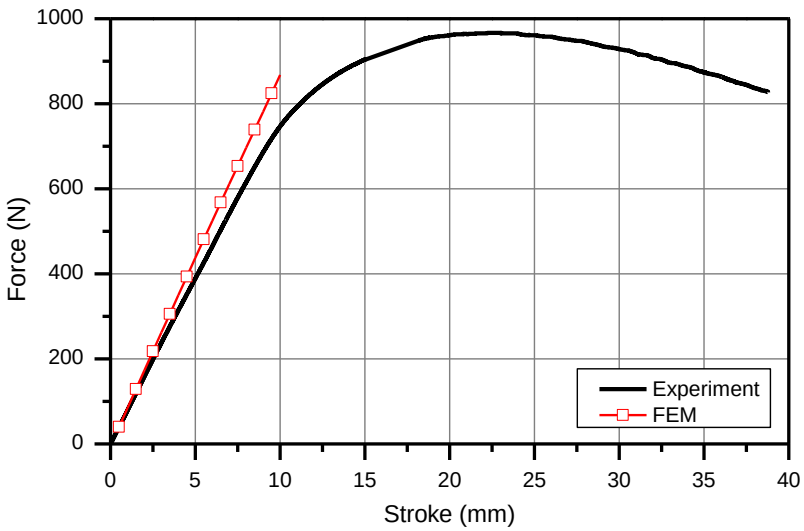

(b)

Figure 8: Force-displacement response comparison of ASA specimen for (a) 3-point bending test, and (b) 4-point bending test.

6. Conclusion

The ultrasonic testing has demonstrated to be a reliable and accurate technique to obtain the orthotropic elastic properties of the FDM-printed ASA material through comparison with the elastic properties obtained from tensile testing and numerical verification with a four-point bending experiment. The elastic properties obtained from ultrasonic testing did not differ much from those obtained from the tensile testing. The small difference between these two sets of properties caused by the difference in the magnitude of the strain rate, however, does not have a significant impact on the finite element simulation of the ASA material. The numerical verification, which was performed using the material properties obtained from the ultrasonic testing, demonstrated excellent correspondence with the experimental results in the three-point and four-point bending tests. Hence, obtaining the elastic properties of 3D printed material using the ultrasonic approach has been proven to be feasible and accurate.

Acknowledgments

This research is jointly supported by the National Research Foundation, Prime Minister's Office, Singapore under its Medium-Sized Centre funding scheme, and ST Engineering Aerospace Ltd., under project titled '3D Printing of UAV Structural Components'.

References

Baumers, M., Dickens, P., Tuck, C., Hague, R., 2016. The cost of additive manufacturing: machine productivity, economies of scale and technology-push. Technological forecasting and social change 102, 193-201.

Cantrell, J.T., Rohde, S., Damiani, D., Gurnani, R., DiSandro, L., Anton, J., Young, A., Jerez, A., Steinbach, D., Kroese, C., Ifju, P.G., 2017. Experimental characterization of the mechanical properties of 3D-printed ABS and polycarbonate parts. Rapid Prototyping Journal 23, 811-824.

Chacón, J.M., Caminero, M.A., García-Plaza, E., Núñez, P.J., 2017. Additive manufacturing of PLA structures using fused deposition modelling: Effect of process parameters on mechanical properties and their optimal selection. Materials & Design 124, 143-157.

Chua, C.K., Wong, C.H., Yeong, W.Y., 2017. Standards, quality control, and measurement sciences in 3D printing and additive manufacturing. Academic Press, London, United Kingdom.

Dawoud, M., Taha, I., Ebeid, S.J., 2016. Mechanical behaviour of ABS: An experimental study using FDM and injection moulding techniques. Journal of Manufacturing Processes 21, 39-45.

Domingo-Espin, M., Puigoriol-Forcada, J.M., Garcia-Granada, A.-A., Llumà, J., Borros, S., Reyes, G., 2015. Mechanical property characterization and simulation of fused deposition modeling Polycarbonate parts. Materials & Design 83, 670-677.

Joshi, S.C., Toh, W., 2011. Elastic Properties of Cnt-Engineered Polymer Composites Using Multi-Level Mechanics Approach. Journal of Multiscale Modelling 03, 271-289.
Lang, S.B., 1970. Ultrasonic Method for Measuring Elastic Coefficients of Bone and Results on Fresh and Dried Bovine Bones. IEEE Transactions on Biomedical Engineering BME-17, 101-105.
Odell, D., Wright, P.K., Montero, M., Roundy, S., Ahn, S.H., 2002. Anisotropic material properties of fused deposition modeling ABS. Rapid Prototyping Journal 8, 248-257.
Peralta, L., Cai, X., Laugier, P., Grimal, Q., 2017. A critical assessment of the in-vitro measurement of cortical bone stiffness with ultrasound. Ultrasonics 80, 119-126.
Sood, A.K., Ohdar, R.K., Mahapatra, S.S., 2010. Parametric appraisal of mechanical property of fused deposition modelling processed parts. Materials & Design 31, 287-295.
Van Buskirk, W.C., Cowin, S.C., Ward, R.N., 1981. Ultrasonic Measurement of Orthotropic Elastic Constants of Bovine Femoral Bone. Journal of Biomechanical Engineering 103, 67-72.
Vashishtha, V.K., Makade, R., Mehla, N., 2011. Advancement of rapid prototyping in aerospace industry-a review. International Journal of Engineering Science and Technology 3, 2486-2493.
Wu, W., Geng, P., Li, G., Zhao, D., Zhang, H., Zhao, J., 2015. Influence of Layer Thickness and Raster Angle on the Mechanical Properties of 3D-Printed PEEK and a Comparative Mechanical Study between PEEK and ABS. Materials 8, 5834-5846.